

REPORT DOCUMENTATION PAGE			Form Approved OMB NO. 0704-0188	
<p>The public reporting burden for this collection of information is estimated to average 1 hour per response, including the time for reviewing instructions, searching existing data sources, gathering and maintaining the data needed, and completing and reviewing the collection of information. Send comments regarding this burden estimate or any other aspect of this collection of information, including suggestions for reducing this burden, to Washington Headquarters Services, Directorate for Information Operations and Reports, 1215 Jefferson Davis Highway, Suite 1204, Arlington VA, 22202-4302. Respondents should be aware that notwithstanding any other provision of law, no person shall be subject to any penalty for failing to comply with a collection of information if it does not display a currently valid OMB control number.</p> <p>PLEASE DO NOT RETURN YOUR FORM TO THE ABOVE ADDRESS.</p>				
1. REPORT DATE (DD-MM-YYYY)		2. REPORT TYPE		3. DATES COVERED (From - To)
		New Reprint		-
4. TITLE AND SUBTITLE			5a. CONTRACT NUMBER	
Subsurface electromagnetic induction imaging for unexploded ordnance detection			W911NF-08-1-0385	
			5b. GRANT NUMBER	
			5c. PROGRAM ELEMENT NUMBER	
6. AUTHORS			5d. PROJECT NUMBER	
Tomasz M. Grzegorzcyk, Juan Pablo Fernández, Fridon Shubitidze, Kevin O'Neill, Benjamin E. Barrowes				
			5e. TASK NUMBER	
			5f. WORK UNIT NUMBER	
7. PERFORMING ORGANIZATION NAMES AND ADDRESSES			8. PERFORMING ORGANIZATION REPORT NUMBER	
Dartmouth College Office of Sponsored Projects Trustees of Dartmouth College Hanover, NH 03753 -1404				
9. SPONSORING/MONITORING AGENCY NAME(S) AND ADDRESS(ES)			10. SPONSOR/MONITOR'S ACRONYM(S) ARO	
U.S. Army Research Office P.O. Box 12211 Research Triangle Park, NC 27709-2211			11. SPONSOR/MONITOR'S REPORT NUMBER(S)	
			55000-EV.1	
12. DISTRIBUTION AVAILABILITY STATEMENT				
Approved for public release; distribution is unlimited.				
13. SUPPLEMENTARY NOTES				
The views, opinions and/or findings contained in this report are those of the author(s) and should not be construed as an official Department of the Army position, policy or decision, unless so designated by other documentation.				
14. ABSTRACT				
Detection and classification of unexploded ordnance based on electromagnetic induction have made tremendous progress over the last few years, to the point that not only more realistic terrains are being considered but also more realistic questions – such as when to stop digging – are being posed. Answering such questions would be easier if it were somehow possible to see under the surface. In this work we propose a method that, within the limitations on resolution imposed in the available range of frequencies, generates subsurface images from which the positions,				
15. SUBJECT TERMS				
Imaging, UXO, subsurface				
16. SECURITY CLASSIFICATION OF:			17. LIMITATION OF ABSTRACT	15. NUMBER OF PAGES
a. REPORT	b. ABSTRACT	c. THIS PAGE	UU	19a. NAME OF RESPONSIBLE PERSON
UU	UU	UU	UU	Fridon Shubitidze
				19b. TELEPHONE NUMBER
				603-646-3671

Report Title

Subsurface electromagnetic induction imaging for unexploded ordnance detection

ABSTRACT

Detection and classification of unexploded ordnance based on electromagnetic induction have made tremendous progress over the last few years, to the point that not only more realistic terrains are being considered but also more realistic questions – such as when to stop digging – are being posed. Answering such questions would be easier if it were somehow possible to see under the surface. In this work we propose a method that, within the limitations on resolution imposed in the available range of frequencies, generates subsurface images from which the positions, relative strengths, and number of targets can be read off at a glance. The method seeds the subsurface with multiple dipoles at known locations that contribute collectively but independently to the measured magnetic field. The polarizabilities of the dipoles are simultaneously updated in a process that seeks to minimize the mismatch between computed and measured fields over a grid. In order to force the polarizabilities to be positive we use their square roots as optimization variables, which makes the problem nonlinear. The iterative update process guided by a Jacobian matrix discards or selects dipoles based on their influence on the measured field. Preliminary investigations indicate a fast convergence rate and the ability of the algorithm to locate multiple targets based on data from various state-of-the-art electromagnetic induction sensors.

REPORT DOCUMENTATION PAGE (SF298)
(Continuation Sheet)

Continuation for Block 13

ARO Report Number 55000.1-EV
Subsurface electromagnetic induction imaging fo ...

Block 13: Supplementary Note

© 2012 . Published in Journal of Applied Geophysics, Vol. Ed. 0 79, (0) (2012), (, (0). DoD Components reserve a royalty-free, nonexclusive and irrevocable right to reproduce, publish, or otherwise use the work for Federal purposes, and to authroize others to do so (DODGARS §32.36). The views, opinions and/or findings contained in this report are those of the author(s) and should not be construed as an official Department of the Army position, policy or decision, unless so designated by other documentation.

Approved for public release; distribution is unlimited.



Subsurface electromagnetic induction imaging for unexploded ordnance detection

Tomasz M. Grzegorzcyk ^{a,*}, Juan Pablo Fernández ^b, Fridon Shubitidze ^c,
Kevin O'Neill ^d, Benjamin E. Barrowes ^{c,d}

^a *Delpsi, LLC, Newton, MA 02458, United States*

^b *88 Franklin St Unit 301, Lynn, MA 01902-4171, United States*

^c *Thayer School of Engineering, Dartmouth College, Hanover, NH 03755-8000, United States*

^d *U.S. Army Corps of Engineers, ERDC/CRREL, Hanover, NH 03755, United States*

ARTICLE INFO

Article history:

Received 10 June 2011

Accepted 30 December 2011

Available online 8 January 2012

Keywords:

Unexploded ordnance
Electromagnetic induction
Subsurface imaging
Gauss–Newton method

ABSTRACT

Detection and classification of unexploded ordnance based on electromagnetic induction have made tremendous progress over the last few years, to the point that not only more realistic terrains are being considered but also more realistic questions – such as when to stop digging – are being posed. Answering such questions would be easier if it were somehow possible to see under the surface. In this work we propose a method that, within the limitations on resolution imposed in the available range of frequencies, generates subsurface images from which the positions, relative strengths, and number of targets can be read off at a glance. The method seeds the subsurface with multiple dipoles at known locations that contribute collectively but independently to the measured magnetic field. The polarizabilities of the dipoles are simultaneously updated in a process that seeks to minimize the mismatch between computed and measured fields over a grid. In order to force the polarizabilities to be positive we use their square roots as optimization variables, which makes the problem nonlinear. The iterative update process guided by a Jacobian matrix discards or selects dipoles based on their influence on the measured field. Preliminary investigations indicate a fast convergence rate and the ability of the algorithm to locate multiple targets based on data from various state-of-the-art electromagnetic induction sensors.

© 2012 Elsevier B.V. All rights reserved.

1. Introduction

Sensing in the electromagnetic induction (EMI) regime of frequencies, which ranges from about 10 Hz to a few hundred kHz, has emerged as an alternative to magnetometry (Billings, 2004) and ground-penetrating radar (Chen et al., 2001) in the search for unexploded ordnance – the most pressing environmental problem faced by the military worldwide (Bilukha et al., 2007; Sethi and Krug, 2000), and one with enormous humanitarian implications – and in general to look for objects buried in the ground (Baum, 1999; Byrnes, 2009). The process in general consists of three stages: (a) Detection – inspect the ground and take a closer look at spots where anomalies are present; (b) Inversion – digest close-interrogation data with a forward model that estimates the location and orientation of the target or targets that cause the anomaly and synthesizes an electromagnetic signature for each; and (c) Classification – distill electromagnetic signatures into intrinsic features that allow the unambiguous characterization of targets, identifying them first and foremost as dangerous ordnance or innocuous scrap and subsequently sorting the unexploded munitions by caliber and type. Headway has been made on all three fronts:

concurrent with the design and assembly of novel sensors that provide data of unprecedented quality and diversity has been the development of several powerful, fast, and accurate data-processing, modeling, and classification algorithms.

On the sensor side, the last few years have seen the appearance of instruments that go well beyond the upright-dipole-transmitter/vertical-component-measuring architecture standard for beachgoing metal detectors. Among cart-based devices, the Time-Domain Electromagnetic Induction Towed Array Detection System (TEM-TADS) developed by the Naval Research Laboratory (Steinhurst et al., 2010) replicates this coplanar/concentric transmitter/receiver paradigm on a 5×5 grid, producing 625 time histories per instrument location, while the Geometrics MetalMapper (Prouty, 2009a; Prouty, 2009b) uses fewer modules but arranges both transmitters and receivers to explore the full three-dimensional vector profile of the field. Hand-based instruments like the Man Portable Vector (MPV) sensor (Barrowes et al., 2011; Fernández et al., 2011) have also incorporated multiple three-axis vector receivers as part of the design and allow sensing in uneven or wooded terrain. These next-generation instruments are ultrawide-band (i.e., they nearly span the complete range of EMI frequencies) and work either in the frequency domain (Fernández et al., 2009; Won et al., 1997; Won et al., 2001) or in the time domain, where they can take readings lasting up to 25 ms after transmitter shutoff.

* Corresponding author.

E-mail address: tomasz.grzegorzcyk@delpsi.com (T.M. Grzegorzcyk).

On the analysis side, several new procedures have either honed or extended the standard model that assumes every target to be a single point dipole (Baum, 1999; Pasion and Oldenburg, 2001). The EMI-response problem has been solved analytically for spheroids (Ao et al., 2002; Barrowes et al., 2004; Braunisch et al., 2001; Chen et al., 2007) and, partially, for ellipsoids (Grzegorzczak et al., 2008). Some semi-analytic models expand the fields in geometrically meaningful modes and solve the problem mode by mode (Fernández et al., 2008; Shubitidze et al., 2004; Sun et al., 2005). Other methods replace the point dipole by surface distributions of magnetic charge (Shubitidze et al., 2007) or dipole moment (Shubitidze et al., 2010a) spread over a surface that encloses the target; more recent versions use volumetric dipole distributions (Shubitidze et al., 2010b). Other possibilities include direct optimizations based on analytical methods (Zhang and Liu, 2001), model-based procedures (Miller et al., 2001), and statistical approaches (Tantum and Collins, 2001).

The resulting combination of hardware and software has been subjected to a battery of tests of increasing realism in places like the former Camp Sibert in Alabama (Fernández et al., 2010b; Shamatava et al., 2009; Shubitidze et al., 2010a), the Aberdeen Proving Ground (APG) in Maryland (Fernández et al., 2010a; Shubitidze et al., 2009), the former Camp San Luis Obispo (SLO) in California (Prouty, 2009a; Prouty, 2009b; Shamatava et al., 2010), and Camp Butner in North Carolina (Shamatava et al., 2011). The results have been consistently encouraging, and for that reason have opened, rather than closed, the need for more sophisticated methods: the UXO community must now consider ever more difficult questions based on acute real-world problems. For example, the need to decontaminate littoral terrain (SanFilipo et al., 2005) has prompted the study of the effects of a conductive embedding medium on EMI sensing. The high densities of both clutter and legitimate targets present in many UXO sites has led to the problem of inverting for the locations and electromagnetic signatures of multiple targets present in the spatial range of a sensor (Grzegorzczak et al., 2009; Song et al., 2009; Grzegorzczak et al., 2011) in order to approximate either multi-UXO configurations or UXO in the presence of a few bulky clutter items. Indeed, it is still not clear how to deal consistently with clutter: questions like how large a piece of clutter should be to be inverted as an additional target, or what density and size distribution a cluster of clutter items should have to be treated as noise rather than a collection of individual objects, are not at all settled.

EMI frequencies (again, between tens of Hz and hundreds of kHz) are useful for subsurface sensing because the ground, with typical conductivity $\sigma \sim 0.1\text{--}1000$ mS/m (though the high end of the range is very rare), permittivity $\epsilon \sim 50\text{--}177$ pF/m, and permeability $\mu \approx \mu_0 \sim 10^{-6}$ H/m, has a skin depth of the order of tens of meters at least and, therefore, is transparent in the range of interest (Keller, 1987; Milsom and Eriksen, 2011). (The values just quoted do not exhaust the very ample ranges in electromagnetic properties exhibited by soils (Butler, 2003), for example in places like Hawai'i, but are representative of the majority of non-littoral soils of interest to the UXO community.) This frequency range, however, is characterized by a very low resolution, which, together with the fact that sensing must be done from a distance, above ground, means that one cannot form any reasonably clear images of the subsurface objects. On the other hand, the available resolution does suffice to locate objects in three dimensions and to resolve targets separated by a few centimeters. This ability – which depends on the sensor employed and on the sizes, orientations, and composition of the relevant targets – opens the possibility of generating subsurface images to aid in the UXO remediation process. In this paper we explore this possibility and propose a methodology to carry it out.

In current practice, responsibility for estimating the number of targets producing a given anomaly falls upon the inversion stage, which typically means that a time-consuming and computationally expensive inversion procedure has to be run either assuming a sequential number of targets (one, two, three, etc.), or assuming an

upper bound on the number of targets, in which case the redundant dipoles either cluster around expected positions or take very small amplitudes that immediately expose them as irrelevant. An increasing number of targets increase the number of model parameters to be inverted and riddles the search space with local minima, making the inversion less reliable and costlier in CPU time – a serious shortcoming in a field where real-time analysis is desirable.

Having a subsurface image, on the other hand, would immediately give operators a set of visual cues to guide their intuition. It would provide an initial estimate of the number of targets, with which it would be possible to run the inversion routine just once; the image would also yield positional information that could accelerate the inversion by providing a sound initial guess for the optimization. The images, moreover, could allow essentially instantaneous anomaly prioritization by allowing the user to pick out the most prominent anomalies, and could also help distinguish between large, deep targets and small, shallow ones. Furthermore, an “imaging” survey at the beginning of the remediation would let operators make educated guesses about the site – i.e., the estimated number and density of dangerous targets, the clutter distribution, the regions to which more attention must be devoted – and thus make more efficient use of their time and resources. In all, an image, as opposed to a beep or a number, makes the detection of UXO more visual and user-friendly, and eventually more reliable because it enables the user to cooperate with the apparatus.

The work presented in (Miller et al., 2010) reports promising results in this direction found using harmony search, a method in which “trials” with a preset number of sources are sequentially generated – either afresh or by making slight changes to existing configurations – and accepted or discarded depending on their “success” – i.e., the closeness of their predictions to measured values. The authors manage to properly resolve multi-target data taken with TEMTADS at the Blossom Point Army Research Facility in Maryland and at APG. The method we propose here is fundamentally different in that it is not stochastic. As in (Miller et al., 2010), we (a) seed the region below the surface with a distribution of point dipoles, each of which contributes to the measured magnetic field, and (b) iteratively update the dipoles' polarizabilities – that is, their dipole moments but dividing out the primary field that induces them – so as to minimize the mismatch between computed and measured fields over a grid, but here the similarities end. Instead of looking for the minimum sufficient number of sources, we look for the sources that have the most influence on the measured data and iteratively “zoom in” on them. Instead of avoiding local minima by occasionally rousting the solution with a random ripple, we use a Jacobian to guide the search downhill. We also force the positivity of the polarizabilities by using their square roots as the parameters to be estimated; this imposition makes the problem nonlinear, but rids the results of trivial solutions and improves convergence to the global minimum.

2. Procedure

Our approach is based on the discretization of the subsurface into dipoles that contribute collectively and independently to the measured magnetic field. The locations of the dipoles are known by construction, but not their polarizabilities, and the task of the algorithm is to compute the polarizabilities that minimize the difference between measured and computed fields. The polarizability amplitudes that result should be high near the true locations of the targets and low everywhere else, allowing the generation of images. There are three polarizability elements per dipole, each of which can either be used by itself to synthesize an image – yielding not just estimates of a target's location but also of its orientation – or combined with the others to form a composite.

As an initial proof of concept we study multitarget ensembles arranged in such a way that it is possible to find a vertical plane that simultaneously cuts either through or close to all of the targets. We then take this plane to define a common and known y -coordinate,

distribute a two-dimensional grid of N_d dipoles on it, and make it our task to synthesize images that let us determine the unknown locations of the targets starting from field data. The restriction to a vertical 2D domain of sources and the placement of the sources on a regular grid have been adopted in this paper for ease of implementation and speed of execution, but neither is a limitation of the method, which we expect to be directly generalizable to 3D configurations. The issues that naturally arise in such generalizations – computational burden, speed, and memory requirements – appear as potential challenges that need to be addressed; this task we postpone to future considerations.

The source dipoles, though constrained to lie in a plane, respond in a fully three-dimensional manner to the primary field of the sensor through the standard expression (Van Bladel, 1964)

$$\bar{H}^d(\bar{r}_o) = \frac{1}{4\pi|\bar{r}|^3} \left(\frac{3\bar{r}(\bar{r} \cdot \bar{m})}{|\bar{r}|^2} - \bar{m} \right), \quad (1)$$

where \bar{r} points from the dipole to the observation point \bar{r}_o and the dipole moment

$$\begin{aligned} \bar{m} &= \hat{x}m_x + \hat{y}m_y + \hat{z}m_z \\ &= \hat{x}\beta_x H_x^{pr} + \hat{y}\beta_y H_y^{pr} + \hat{z}\beta_z H_z^{pr}, \end{aligned} \quad (2)$$

with \bar{H}^{pr} the primary field at the location of the dipole. The polarizabilities β_ξ , $\xi \in \{x, y, z\}$, are in general elements of a symmetric 3×3 tensor. We force the principal axes of all the dipoles to coincide with those of the sensor, resulting in a diagonal polarizability tensor with only three nonzero values. We thus set out to solve

$$\begin{aligned} \min_{\{\beta_\xi\}} & \left\| \sum_j \frac{1}{4\pi|\bar{r}_j|^3} \left(\frac{3\bar{r}_j \bar{r}_j}{|\bar{r}_j|^2} - \bar{I} \right) \cdot \bar{m}_j - \bar{H}^{\text{meas}} \right\|_2 \\ \text{s.t.} & \quad \{\beta_\xi\} > 0 \quad \forall \xi, \end{aligned} \quad (3)$$

where we have enclosed the β_ξ in curly brackets to emphasize that the minimization involves all N_d seeded dipoles and have strung together the measured fields in the vector

$$\bar{H}^{\text{meas}} \equiv \begin{bmatrix} \bar{H}_1^{\text{meas}} \\ \vdots \\ \bar{H}_N^{\text{meas}} \end{bmatrix} \quad (4)$$

of length $N \cdot N_{\text{cmp}} \equiv (N_{\text{loc}} \cdot N_{\text{Tx}} \cdot N_{\text{Rx}}) \cdot N_{\text{cmp}}$, where N_{loc} is the number of sensor locations at which data are collected, N_{Tx} and N_{Rx} are respectively the number of transmitters and receivers on the sensor, and N_{cmp} is the number of measured field components. We also have made explicit the fact that the polarizabilities are always positive (Pasion et al., 2008); we impose this constraint in the minimization by using the square roots of the polarizabilities, $\gamma_\xi = \sqrt{\beta_\xi}$, as inversion parameters:

$$\begin{aligned} \min_{\{\gamma_\xi\}} & \left(\left\| \sum_j \bar{G}(\bar{r}_j) \mathbf{y}_j - \bar{H}^{\text{meas}} \right\|_2 + \|\lambda \mathbf{y}\|_2 \right) \\ & \equiv \min_{\{\gamma_\xi\}} (\|\Delta \bar{H}(\mathbf{y})\|_2 + \|\lambda \mathbf{y}\|_2), \end{aligned} \quad (5)$$

where

$$\mathbf{y}_j = \begin{bmatrix} \gamma_{x,j}^2 \\ \gamma_{y,j}^2 \\ \gamma_{z,j}^2 \end{bmatrix}, \quad \mathbf{y} = \begin{bmatrix} \mathbf{y}_1 \\ \vdots \\ \mathbf{y}_{N_d} \end{bmatrix}, \quad (6)$$

the Green dyads \bar{G} incorporate the dipole contributions from Eq. (3) with the primary field factored in, and $\Delta \bar{H}$ stands for the mismatch between modeled and measured signals. Using γ_ξ as the variables instead of β_ξ makes the problem nonlinear, one that has to be solved iteratively.

We use a Gauss–Newton method (Press et al., 1992) for the task, regularized with a Tikhonov term in order to give preferential weight to solutions with smaller norms (Aster et al., 2005). The $3N_d \times 1$ solution vector \mathbf{x} , equivalent to the elementwise square root of \mathbf{y} , is formally the limit as $i \rightarrow \infty$ of an iteration-dependent \mathbf{x}^i . The initial value \mathbf{x}^0 is chosen at random, though making reasonable assumptions (e.g., that the polarizabilities have roughly the same order of magnitude), and each subsequent update to the vector comes from solving the normal equation

$$\mathbf{x}^{i+1} = \mathbf{x}^i + \left(\bar{J}^T \bar{J} + \lambda \bar{I} \right)^{-1} \bar{J}^T \Delta \bar{H}(\mathbf{x}^i), \quad (7)$$

where the i -dependent $N \cdot N_{\text{cmp}} \times 3N_d$ Jacobian

$$\bar{J} = \begin{bmatrix} \partial \bar{H}_1 / \partial \mathbf{x}^i \\ \partial \bar{H}_2 / \partial \mathbf{x}^i \\ \vdots \\ \partial \bar{H}_N / \partial \mathbf{x}^i \end{bmatrix} \quad (8)$$

guides the search by approximating the Hessian (Gill et al., 1981). The derivatives with respect to the square roots of the polarizabilities are straightforward to compute, given the simple dependence of Eq. (1) on the $\{\beta\}$. The Tikhonov regularization parameter λ (Hansen, 2010) is initially chosen so that the condition number of the regularized approximate Hessian matrix $(\bar{J}^T \bar{J} + \lambda \bar{I})$ is no less than 10^{-10} , and then adjusted at every iteration using

$$\lambda = \frac{\zeta}{N_d} \text{Tr} \left\{ \bar{J}^T \bar{J} \right\} \left\| \Delta \bar{H}(\mathbf{x}^i) \right\|_2^2, \quad (9)$$

where ζ is adjustable (we use $\zeta = 10^{-4}$ throughout this paper). At the outset the matrices are ill-conditioned, and the regularization term helps stabilize the inversion; as the iteration progresses, the field mismatch $\Delta \bar{H}$ tends to zero and λ becomes ever less important compared to the data.

Once the process converges we look for the region with the highest concentration of polarizability amplitude and zoom in on it with the aim of generating more finely detailed images. Restricting our attention to the smaller computational space, we distribute a similar grid of dipoles and perform a new optimization. This refocusing helps us keep a moderate number of source dipoles and makes for a more efficient algorithm; let us also emphasize that no additional sensor data are required. The process is repeated until we obtain a “polarizability map,” with high concentrations of polarizability being indicative of target location. At this stage, the refocusing is performed manually, by eye, but it is not hard to envision how the process could be automated.

3. Results

We have performed initial validating studies of our algorithm using both synthetic and measured data. The synthetic data incorporate the geometries of current sensors and targets with realistic signatures and locations.

3.1. Synthetic scenarios

Initially we compare the images that can be obtained when the algorithm has access to full three-dimensional magnetic-field data and when only the vertical component is available. For definiteness we consider a TEMTADS-like configuration: we generate images starting from a single data shot as collected by 25 receivers distributed on a 5×5 rectangular uniform grid, with each receiver separated from its neighbors center-to-center by 40 cm. The sensor is assumed to lie centered at the origin and flat on the ground. To simulate unfavorable measurement conditions, we take only a subset of the data that can possibly be collected by the instrument: though each TEMTADS receiver is concentric with a transmitter, we use the data collected when only the

center transmitter is fired. The targets are two point dipoles placed at $x = \pm 10$ cm at a depth of 50 cm below the sensor center and oriented along \hat{z} with unit magnitude (hence $\beta_x = \beta_y = 0, \beta_z = 1$ for each dipole). A set of 50×50 source dipoles are distributed on a two-dimensional vertical grid on the $y = 0$ plane spanning 2 m (the side length of TEMTADS) along the x -direction and going from 20 cm to 1 m in depth. Figs. 1 and 2 respectively report the results found using all three components of \vec{H} and using H_z only. The figures present the normalized polarizability magnitude of the j th dipole, computed using

$$\beta_j = \tilde{\beta}_j / \max_j(\tilde{\beta}_j), \quad \tilde{\beta}_j = \sqrt{\beta_{xj}^2 + \beta_{yj}^2 + \beta_{zj}^2}, \quad j = 1, \dots, N_d. \quad (10)$$

The bottom-right panels in the figures illustrate the typical convergence rate of our algorithm by showing how the normalized error evolves as a function of the iteration number. Note that in Figs. 1 and 2 the pixel amplitudes of images corresponding to $\{\beta_x\}$ and $\{\beta_y\}$ are negligible compared to those corresponding to $\{\beta_z\}$, as expected, and are not shown. The colors in the figures range from blue to red, corresponding to respective amplitudes of zero and one, with a similar format adopted for all subsequent figures. The figures illustrate the fact that polarizability amplitudes are much stronger close to the target locations than everywhere else, where they are essentially zero. Physical information on dipole strength can be obtained by integrating the images.

Though in both cases the targets are properly resolved and found at locations not far from the ground truth – denoted in the figures by white circles – it is not surprising that the objects are easier to discern in the former situation: just one zoom is necessary to resolve properly

the targets in Fig. 1, while they remain poorly separated in the case of Fig. 2.

We remind the reader that this hypothetical exercise aims to study the effect of using one vs. three components of the magnetic field and is not expected to be generalized to the actual TEMTADS sensor array, which provides 625 data points rather than the 25 we use here. A realistic TEMTADS case is considered below.

As a second example, we consider a situation in which a weaker dipole (which could represent a clutter item) is buried at a shallow depth above a deeper yet stronger target that could stand for UXO. This is a common occurrence in the field, and one that time and again has proved difficult to analyze. We use the same TEMTADS-like configuration from the previous example and use all components of the magnetic field. The targets are placed 10 cm to the right of the simulated sensor in the x -direction and centered in y ; the “clutter” target is at a depth of 20 cm; the “UXO” target is 30 cm deeper and its dipole moment has twice the magnitude. Both objects are oriented along \hat{z} . The source dipoles are on the same initial grid as in the previous example. The results, which appear in Fig. 3, again reveal that the algorithm can identify the region in which targets are present and can distinguish the shallow object from the deeper, stronger one.

3.2. Experimental configurations

We subsequently illustrate the performance of our algorithm on actual measurements taken with three different state-of-the-art EMI sensors: the TEMTADS array (Steinhurst et al., 2010), the MPV sensor (Fernández et al., 2011; George and George, 2007), and the Metal-Mapper system (Prouty, 2009a). Each of these sensors presents a

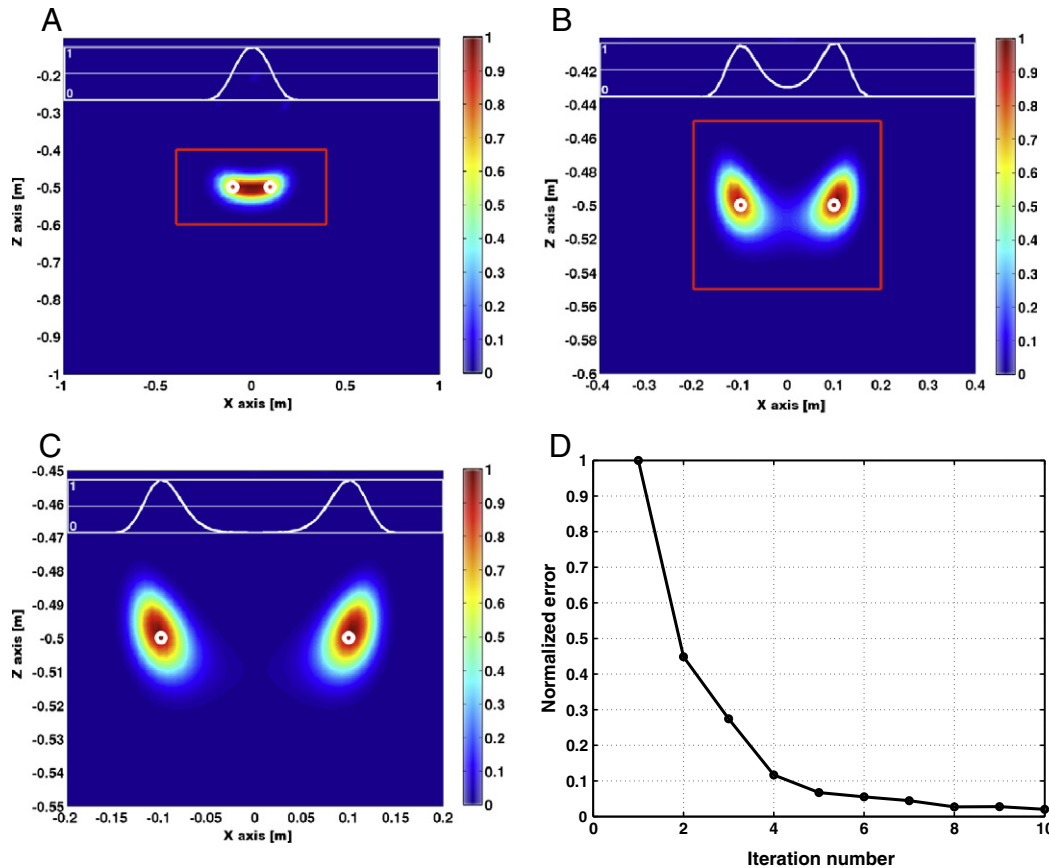


Fig. 1. Image based on synthetic data generated over a 5×5 grid similar to that of TEMTADS but using only one transmit coil. Two dipoles of similar moment are placed at the locations indicated by the white circles. All vector components of the polarizabilities are added pixel-to-pixel to generate the image. Pixel amplitudes are normalized between 0 (blue) and 1 (red). *Top-left:* First stage with large initial region. *Top-right:* Second stage and refocusing within the red rectangle of (A). *Bottom-left:* Third stage and refocusing within the red rectangle of (B). *Bottom-right:* Normalized error as a function of the iteration number for (A).

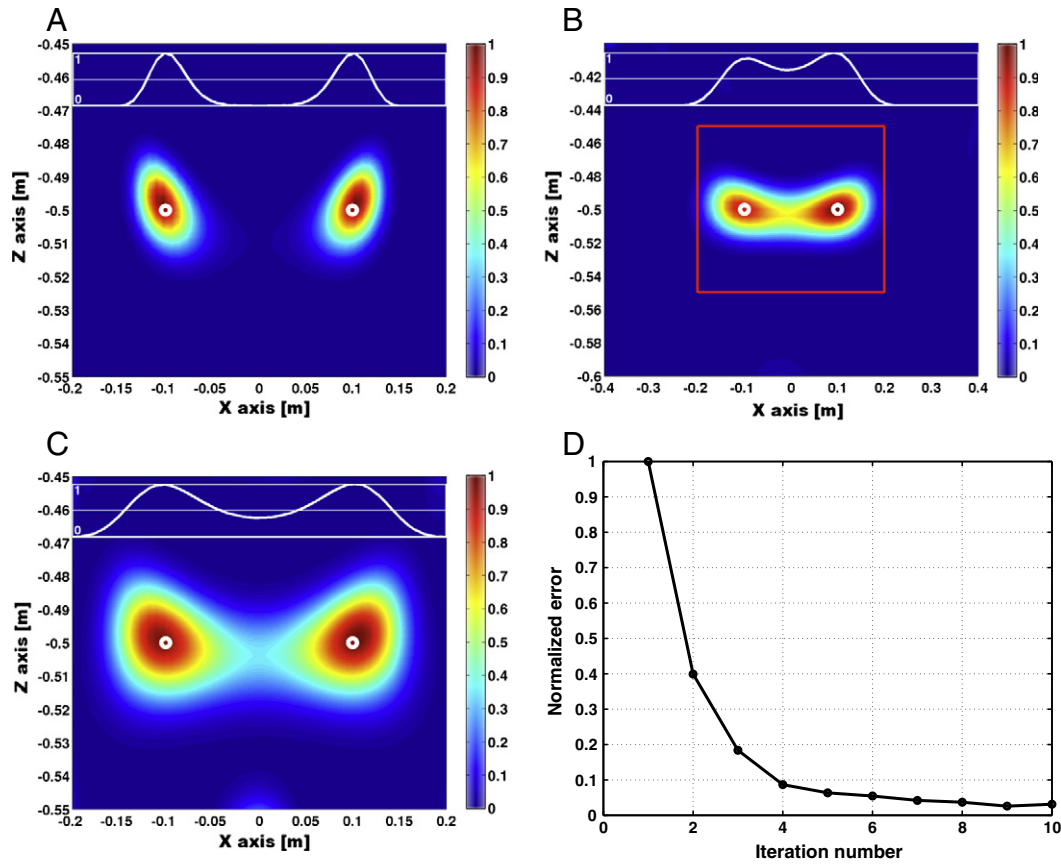


Fig. 2. Same as Fig. 1 but using only the \hat{z} -component of the magnetic field. It is seen that two refocusing stages are needed to resolve the two sources. Pixel amplitudes are normalized between 0 (blue) and 1 (red). *Top-left*: First stage with large initial region. *Top-right*: Second stage and refocusing within the red rectangle of (A). *Bottom-left*: Third stage and refocusing within the red rectangle of (B). *Bottom-right*: Normalized error as a function of the iteration number for (A).

different transmit/receive configuration that is unique enough to warrant independent processing with our algorithm.

3.2.1. TEMTADS data

The TEMTADS array, already described above, is composed of a 5×5 square grid of parallel coplanar flat transmitter/receiver pairs. A total of 625 measurements, corresponding to each transmitter/receiver combination, are available for analysis at each sensor location, and the 40-cm

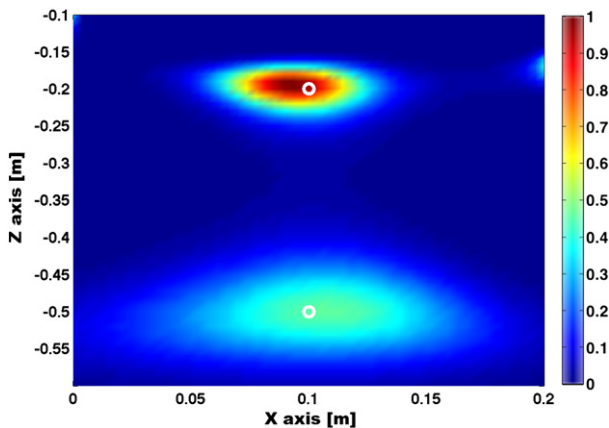


Fig. 3. Normalized polarizability map obtained from synthetic data generated over a TEMTADS-like 5×5 grid with a single transmit coil. Two dipoles are placed on top of each other at $(10, 0, -20)$ cm and $(10, 0, -50)$ cm, as indicated by the white circles. The shallow dipole has half the strength of the deeper one. The images are presented as a single polarizability magnitude obtained from Eq. (10).

neighbor-to-neighbor separation generates data of enough diversity in viewpoint to make up for the fact that only the z -component of the field is measured.

Our TEMTADS example has three targets on the x - z plane: a mortar buried 60 cm below the origin and pointing along \hat{x} , a baseplate at a depth of 44 cm and 50 cm to the left of the mortar, and a nosepiece buried 29 cm below ground and 20 cm to the left of the baseplate (see Fig. 4). In a previous paper (Grzegorzczak et al., 2011) we analyzed this same configuration, estimating the locations, orientations, and entire time-dependent polarizabilities of all three targets using a full inversion/discrimination algorithm but knowing a priori the number of buried targets. In the present work we make no assumptions about the number of targets but attempt to estimate it from the image itself. In addition, we focus on target location and not on time-dependent signatures, and for that reason run the imaging algorithm on a single time channel, typically an early one with high signal-to-noise ratio.

The subsurface in this example is seeded with 40×40 dipoles over a uniformly distributed rectangular grid on the $y = 0$ plane spanning between -1 m and $+1$ m in the x -direction and between 10 cm and 1 m in depth. The uniform dipole distribution is not a requirement of the algorithm but merely reflects the fact that we assume no previous knowledge about the configuration beyond the shared y -location. The algorithm is run with 10 iterations and produces the results shown in Fig. 4. The superposed white circles indicate the ground truth. Overall we see a good match between the actual target locations and the peaks in polarizability; the background is seen to be void of spurious sources. We note that the nosepiece, despite being the target closest to TEMTADS, is the most difficult to find; we attribute the inaccuracy to the nosepiece's being almost at the edge of the sensor and therefore interrogated from relatively few angles.

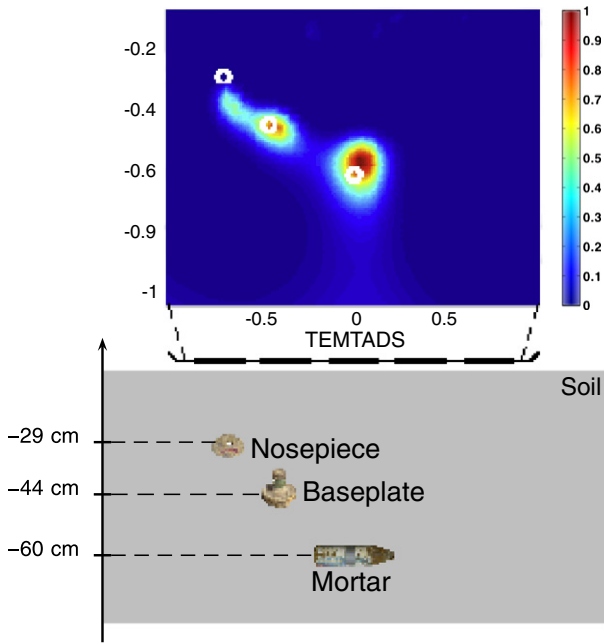


Fig. 4. Configuration and resulting normalized polarizability map obtained from a three-target TEMTADS measurement. The targets are as follows: mortar at (0,0,-60) cm, baseplate at (-50,0,-44) cm, and nose piece at (-70,0,-29) cm. Axes dimensions of the image are in meters.

3.2.2. MPV data

As its name indicates, the MPV (described in more detail elsewhere (Fernández et al., 2011)) is a man-portable and therefore much smaller sensor. It has a single horizontal transmit direction for the primary field but captures all three components of the secondary field at five locations, one of them at a different height than the others. The field of view is consequently much smaller than that of TEMTADS, though this limitation (as well as the lack of primary-field diversity) could be overcome by waving the instrument around and tilting it above an anomaly. This, however, is not attempted here.

Our MPV example has two 40-mm UXO within the area scanned by the sensor, located at the same depth of 40 cm and separated by a lateral distance also of 40 cm. The data were collected by Sky Research personnel in Hanover, New Hampshire, using a 5x5 uniform square grid of side 80 cm and a point-to-point separation of 20 cm. The algorithm is run using a uniform 40x40 dipole distribution seeded on the x-z plane and confined to a lateral region between -50 cm and +50 cm in \hat{x} and between 10 cm and 50 cm in depth. The result, shown in Fig. 5, reveals the presence of two targets at locations that match the ground truth (white circles) well.

3.2.3. MetalMapper data

As a final example, we consider data collected by the MetalMapper in a test mode at Camp San Luis Obispo (Prouty, 2009a; Prouty, 2009b). The instrument has three mutually perpendicular transmitter coils and seven receiver cubes that measure all three vector components of the secondary field. The dataset is therefore rich in information, though geometrically more restricted than those achievable with TEMTADS. The targets are two copper rings, each of 19 cm and 21 cm inner and outer diameters and otherwise thin. One is buried flat under the first quadrant of the sensor; the other is placed vertically under the fourth quadrant (see Fig. 6). The geometry of the latter target makes it difficult to induce eddy currents in it with a less flexible instrument.

The algorithm employs 40x40 dipoles uniformly distributed between -0.7 m and +0.7 m in \hat{x} and between -0.6 m and -0.1 m in \hat{z} . The image of Fig. 7 results after ten iterations. As we state at the beginning of Section 2, the procedure produces three images, one along

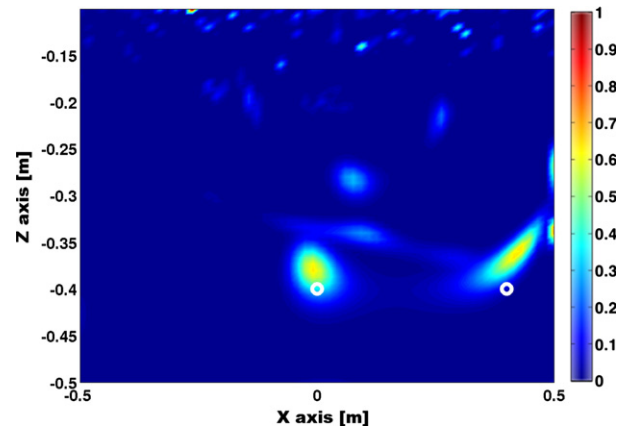


Fig. 5. Normalized polarizability map obtained from a two-target MPV measurement. The buried objects are two identical 40-mm projectiles located at (0,0,-40) cm and (40,0,-40) cm. In this case there is no need to “refocus” the algorithm.

each canonical direction. The thin rings will tend to be visible only along the direction where it is possible to induce currents in them, which means that each of them would appear in only one of the images. Fig. 7 has been obtained, as elsewhere in this paper, by computing the normalized polarizability magnitude of (10). Both targets are seen to be properly located when compared to estimates from two independent full inversions (which again appear as white circles). We do note that the method overestimates the depth of the deeper target by a few centimeters.

4. Conclusion

In this paper we have presented a method that could be used to generate subsurface images and locate unexploded ordnance using already available EMI sensors. As validating examples we studied several multi-target configurations, some synthetically generated and others measured by the TEMTADS, MPV, and MetalMapper next-generation systems. The accuracy of our results suggests that the method has the flexibility required to process varied datasets adequately, including those with scalar/vector transmitters and/or scalar/vector receivers. Moreover, our algorithm uses the data already provided by existing

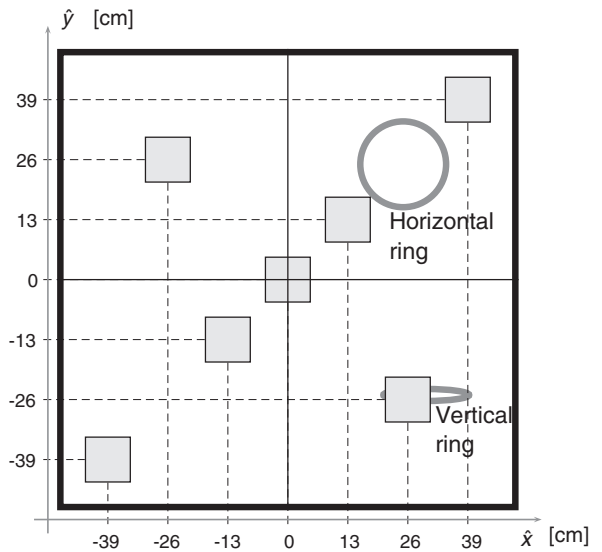


Fig. 6. Schematic representation of the \hat{z} MetalMapper transmitting coil, the seven vector receivers, and the positions of the horizontal and vertical rings. The other transmitters are perpendicular to the \hat{x} and \hat{y} directions and are centered 56 cm above the plane of the sheet.

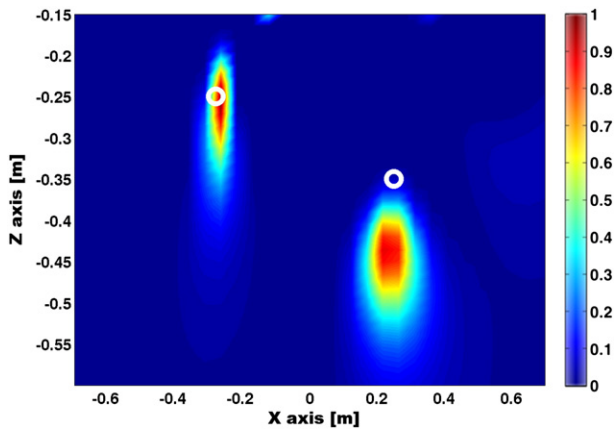


Fig. 7. Two-target normalized polarizability map obtained from the MetalMapper data.

sensors and requires nothing more. We believe that this method could be incorporated into current systems and in that capacity prove beneficial to the field teams in charge of locating and eventually unearthing UXO.

The proof of concept presented in this paper has concentrated on 2D situations, with all targets sharing a known y -coordinate. The generalization to 3D imaging is conceptually straightforward, given that the method is already three-dimensional in nature, but the expected increase in computational needs poses challenges that may require investigation of acceleration methods.

Other limitations of the model also need to be investigated quantitatively before the technology is mature enough for field deployment. In particular, resolvability with respect to realistic levels of noise in EMI data needs to be characterized in order to quantify how small, how deep, and (in multi-target cases) how closely clustered subsurface objects can be and still be resolvable.

Results are expected to vary not only with the level of noise associated with EMI measurements and instrument positioning, but also with the accuracy with which the background can be canceled. In our experience, real-field situations are very diverse, and resolvability should be studied on a case-by-case basis; for that reason we decided against adding synthetic, one-size-fits-all noise to the synthetic cases present in this paper. Finally, it would be desirable to incorporate into the model the time evolution of signals, given its potential usefulness as a discrimination tool. Such considerations represent the next steps to take based on the results we have presented here.

Acknowledgment

This material is based upon work supported by the U. S. Army Corps of Engineers, Humphreys Engineer Center Support Activity, under Contract No. W912HQ-11-C-0072 and the U. S. Army Corps of Engineers, Engineer Research and Development Center, Cold Regions Research and Engineering Laboratory, under Contracts Nos. W913E5-11-C-0014 and W913E5-10-C-0016. The authors would like to thank S. Jensen-Segal and I. Shamatava of Sky Research for providing the MPV data of Section 3.2.2, M. Prouty of Geometrics, Inc., D. C. George of G&G Sciences and D. D. Snyder of Snyder Geoscience for providing the MetalMapper data of Section 3.2.3, and D. A. Steinhurst of Nova Research for providing the TEMTADS data of Section 3.2.1.

References

Ao, C.O., Braunisch, H., O'Neill, K., Kong, J.A., 2002. Quasi-magnetostatic solution for a conducting and permeable spheroid with arbitrary excitation. *IEEE Transactions on Geoscience and Remote Sensing* 40, 887–897.

Aster, R.C., Borchers, B., Thurber, C.H., 2005. *Parameter Estimation and Inverse Problems*. Elsevier, Burlington, MA.

Barrowes, B.E., O'Neill, K., Grzegorzczak, T.M., Chen, X., Kong, J.A., 2004. Broadband analytical magnetoquasistatic electromagnetic induction solution for a conducting and permeable spheroid. *IEEE Transactions on Geoscience and Remote Sensing* 42, 2479–2489.

Barrowes, B.E., et al., 2011. Portable electromagnetic induction sensor with integrated positioning. SERDP Project MR-1712 Report. CRREL/Dartmouth College, Hanover, NH. <http://www.serdp.org/Program-Areas/Munitions-Response/Land/Sensors/MR-1712>.

Baum, C.E. (Ed.), 1999. *Detection and Identification of Visually Obscured Targets*. Taylor & Francis, Philadelphia.

Billings, S.D., 2004. Discrimination and classification of buried unexploded ordnance using magnetometry. *IEEE Transactions on Geoscience and Remote Sensing* 42, 1241–1251.

Bilukha, O.O., Brennan, M., Anderson, M., 2007. Injuries and deaths from landmines and unexploded ordnance in Afghanistan, 2002–2006. *Journal of the American Medical Association* 298, 516–518.

Braunisch, H., Ao, C.O., O'Neill, K., Kong, J.A., 2001. Magnetoquasistatic response of conducting and permeable prolate spheroid under axial excitation. *IEEE Transactions on Geoscience and Remote Sensing* 39, 2689–2701.

Butler, D.K., 2003. Implications of magnetic backgrounds for unexploded ordnance detection. *Journal of Applied Geophysics* 54, 111–125.

Byrnes, J. (Ed.), 2009. *Unexploded Ordnance Detection and Mitigation*. Springer Netherlands, Dordrecht.

Chen, C.C., Higgins, M.B., O'Neill, K., Detsch, R., 2001. Ultrawide-bandwidth fully-polarimetric ground penetrating radar classification of subsurface unexploded ordnance. *IEEE Transactions on Geoscience and Remote Sensing* 39, 1221–1230.

Chen, X., O'Neill, K., Grzegorzczak, T.M., Kong, J.A., 2007. Spheroidal mode approach for the characterization of metallic objects using electromagnetic induction. *IEEE Transactions on Geoscience and Remote Sensing* 45, 697–706.

Fernández, J.P., Barrowes, B.E., O'Neill, K., Shamatava, I., Shubitidze, F., Sun, K., 2008. A data-derived time-domain SEA for UXO identification using the MPV sensor. In: Harmon, R.S., Broach, J.T., Holloway Jr., J.H. (Eds.), *Detection and Sensing of Mines, Explosive Objects, and Obscured Targets XIII*, Bellingham, WA, 69531H.

Fernández, J.P., Barrowes, B.E., O'Neill, K., Shamatava, I., Shubitidze, F., 2009. A vector handheld frequency-domain sensor for UXO identification. In: Harmon, R.S., Broach, J.T., Holloway Jr., J.H. (Eds.), *Detection and Sensing of Mines, Explosive Objects, and Obscured Targets XIV*, Bellingham, WA, 73030W.

Fernández, J.P., Barrowes, B.E., Bijamov, A., Grzegorzczak, T., Shamatava, I., O'Neill, K., Shubitidze, F., 2010a. Combining electromagnetic induction and automated classification in a UXO discrimination blind test. In: Harmon, R.S., Broach, J.T., Holloway Jr., J.H. (Eds.), *Detection and Sensing of Mines, Explosive Objects, and Obscured Targets XV*, Bellingham, WA, 766403.

Fernández, J.P., Barrowes, B.E., O'Neill, K., Shamatava, I., Shubitidze, F., 2010b. Realistic subsurface anomaly discrimination using electromagnetic induction and an SVM classifier. *EURASIP Journal of Advance and Signal Processing* 2010, 305890.

Fernández, J.P., Barrowes, B.E., Grzegorzczak, T.M., Lhomme, N., O'Neill, K., Shubitidze, F., 2011. A man-portable vector sensor for identification of unexploded ordnance. *IEEE Sensors Journal* 11, 2542–2555.

George, D.C., George, J.L., 2007. Data report: Tests of MPV at Vicksburg, February 26 to March 2, 2007. Technical Note 2007–2. G&G Sciences Inc, Grand Junction, CO. <http://www.ggsciences.com>.

Gill, P.E., Murray, W., Wright, M.H., 1981. *Practical Optimization*. Academic Press.

Grzegorzczak, T.M., Zhang, B., Kong, J.A., Barrowes, B.E., O'Neill, K., 2008. Electromagnetic induction from highly permeable and conductive ellipsoids under arbitrary excitation: application to the detection of unexploded ordnances. *IEEE Transactions on Geoscience and Remote Sensing* 46, 1164–1176.

Grzegorzczak, T.M., Barrowes, B., Shubitidze, F., Fernández, J.P., Shamatava, I., O'Neill, K., 2009. Detection of multiple subsurface metallic targets using EMI data. In: Harmon, R.S., Broach, J.T., Holloway Jr., J.H. (Eds.), *Detection and Sensing of Mines, Explosive Objects, and Obscured Targets XIV*, Bellingham, WA, 73030T.

Grzegorzczak, T.M., Barrowes, B.E., Shubitidze, F., Fernández, J.P., O'Neill, K., 2011. Simultaneous identification of multiple unexploded ordnance using electromagnetic induction sensors. *IEEE Transactions on Geoscience and Remote Sensing* 49, 2507–2517.

Hansen, P.C., 2010. *Discrete Inverse Problems: Insight and Algorithms*. SIAM, Philadelphia.

Keller, G.V., 1987. Rock and mineral properties. In: Nabighian, M.N. (Ed.), *Electromagnetic Methods in Applied Geophysics*. Society of Exploration Geophysicists, 1. Tulsa, OK, pp. 13–51.

Miller, J.T., Bell, T.H., Soukup, J., Keiswetter, D., 2001. Simple phenomenological models for wideband frequency-domain electromagnetic induction. *IEEE Transactions on Geoscience and Remote Sensing* 39, 1294–1298.

Miller, J.T., Keiswetter, D., Kingdon, J., Furuya, T., Barrow, B., Bell, T., 2010. Source separation using sparse-solution linear solvers. In: Harmon, R.S., Broach, J.T., Holloway Jr., J.H. (Eds.), *Detection and Sensing of Mines, Explosive Objects, and Obscured Targets XV*, Bellingham, WA, 766409.

Millsom, J., Eriksen, A., 2011. *Field Geophysics*, 4th edition. Wiley-Blackwell, Chichester, UK.

Pasion, L.R., Oldenburg, D.W., 2001. A discrimination algorithm for UXO using time-domain electromagnetic induction. *Journal of Environmental and Engineering Geophysics* 6, 91–102.

Pasion, L.R., Billings, S.D., Kingdon, K.A., Oldenburg, D.W., Lhomme, N., Jacobson, J., 2008. Cooperative inversion of time domain electromagnetic and magnetometer data for the discrimination of unexploded ordnance. *Journal of Environmental and Engineering Geophysics* 13, 193–210.

Press, W.H., Teukolsky, S.A., Vetterling, W.A., Flannery, B.P., 1992. *Numerical Recipes in C*, 2nd edition. Cambridge Univ. Press, Cambridge, UK.

- Prouty, M., 2009a. Detection and classification with the MetalMapper™ at former Camp San Luis Obispo. ESTCP Project MM-0603 Draft Demonstration Plan. Geometrics, Inc, San Jose, CA. <http://www.geometrics.com>.
- Prouty, M., 2009b. MetalMapper system: Camp San Luis Obispo discrimination study. ESTCP Project MM-0603 Interim Data Report. Geometrics, Inc, San Jose, CA. <http://www.serdp-estcp.org/Program-Areas/Munitions-Response/Land/Sensors/MR-200603/>.
- SanFilipo, W.A., Norton, S.J., Won, I.J., 2005. The effects of seawater on the EMI response of UXO. *Oceans* 2005, 607–614.
- Sethi, D., Krug, E. (Eds.), 2000. *Guidance for Surveillance of Injuries Due to Landmines and Unexploded Ordnance*. World Health Organization, Geneva.
- Shamatava, I., Shubitidze, F., Barrowes, B.E., Fernández, J.P., Pasion, L.R., O'Neill, K., 2009. Applying the physically complete EMI models to the ESTCP Camp Sibert Pilot Study EM-63 data. In: Harmon, R.S., Broach, J.T., Holloway Jr., J.H. (Eds.), *Detection and Sensing of Mines, Explosive Objects, and Obscured Targets XIV*, Bellingham, WA, 730300.
- Shamatava, I., Shubitidze, F., Fernández, J.P., Barrowes, B.E., O'Neill, K., Grzegorzczak, T.M., Bijamov, A., 2010. SLO blind data set inversion and classification using physically complete models. In: Harmon, R.S., Broach, J.T., Holloway Jr., J.H. (Eds.), *Detection and Sensing of Mines, Explosive Objects, and Obscured Targets XV*, Bellingham, WA, 766404.
- Shamatava, I., Shubitidze, F., Fernández, J.P., Barrowes, B.E., O'Neill, K., Bijamov, A., 2011. Live-site UXO classification studies using advanced EMI and statistical models. In: Harmon, R.S., Holloway Jr., J.H., Broach, J.T. (Eds.), *Detection and Sensing of Mines, Explosive Objects, and Obscured Targets XVI*, Bellingham, WA, 801709.
- Shubitidze, F., O'Neill, K., Shamatava, I., Sun, K., Paulsen, K.D., 2004. A standardized excitation approach for classification of buried UXO. 2004 IEEE International Geoscience & Remote Sensing Symposium, 4905–4908.
- Shubitidze, F., O'Neill, K., Barrowes, B.E., Shamatava, I., Sun, K., Fernández, J.P., Paulsen, K.D., 2007. Application of the normalized surface magnetic charge model to UXO discrimination in cases with overlapping signals. *Journal of Applied Geophysics* 61, 292–303.
- Shubitidze, F., Barrowes, B.E., Fernández, J.P., Shamatava, I., O'Neill, K., 2009. APG UXO discrimination studies using advanced EMI models and TEMTADS data. In: Harmon, R.S., Broach, J.T., Holloway Jr., J.H. (Eds.), *Detection and Sensing of Mines, Explosive Objects, and Obscured Targets XIV*, Bellingham, WA, 73030M.
- Shubitidze, F., Fernández, J.P., Shamatava, I., Pasion, L.R., Barrowes, B.E., O'Neill, K., 2010a. Application of the Normalized Surface Magnetic Source model to a blind unexploded ordnance discrimination test. *ACES Journal* 25, 89–98.
- Shubitidze, F., Karkashadze, D., Fernández, J.P., Barrowes, B.E., O'Neill, K., Grzegorzczak, T., Shamatava, I., 2010b. Applying a volume dipole distribution model to next-generation sensor data for multi-object data inversion and discrimination. In: Harmon, R.S., Broach, J.T., Holloway Jr., J.H. (Eds.), *Detection and Sensing of Mines, Explosive Objects, and Obscured Targets XV*, Bellingham, WA, 766407.
- Song, L.P., Oldenburg, D.W., Pasion, L.R., Billings, S.D., 2009. Transient electromagnetic inversion for multiple targets. In: Harmon, R.S., Broach, J.T., Holloway Jr., J.H. (Eds.), *Detection and Sensing of Mines, Explosive Objects, and Obscured Targets XIV*, Bellingham, WA, 73030R.
- Steinhurst, D.A., Harbaugh, G.R., Kingdon, J.B., Furuya, T., Keiswetter, D.A., George, D.C., 2010. EMI array for cued UXO discrimination. ESTCP Project MM-0601 Final Report. <http://www.serdp.org/Program-Areas/Munitions-Response/Land/Sensors/MR-200601/MR-200601>.
- Sun, K., O'Neill, K., Shubitidze, F., Shamatava, I., Paulsen, K., 2005. Fast data-derived fundamental spheroidal excitation models with application to UXO discrimination. *IEEE Transactions on Geoscience and Remote Sensing* 43, 2573–2583.
- Tantum, S.L., Collins, L.M., 2001. A comparison of algorithms for subsurface target detection and identification using time-domain electromagnetic induction data. *IEEE Transactions on Geoscience and Remote Sensing* 39, 1299–1306.
- Van Bladel, J., 1964. *Electromagnetic Fields*. McGraw-Hill, New York.
- Won, I.J., Keiswetter, D.A., Hanson, D.R., Novikova, E., Hall, T.M., 1997. GEM-3: a monostatic broadband electromagnetic induction sensor. *Journal of Environmental and Engineering Geophysics* 2, 53–64.
- Won, I.J., Keiswetter, D.A., Bell, T.H., 2001. Electromagnetic induction spectroscopy for clearing landmines. *IEEE Transactions on Geoscience and Remote Sensing* 39, 703–709.
- Zhang, Z.Q., Liu, Q.H., 2001. Two nonlinear inverse methods for electromagnetic induction measurements. *IEEE Transactions on Geoscience and Remote Sensing* 39, 1331–1339.